

High-frequency complex impedance analysis of the two-dimensional semiconducting MXene-Ti₂CO₂

Anup Kumar Mandia^a, Rohit Kumar^a, Namitha Anna Koshi^b, Seung-Cheol Lee^c, Satadeep Bhattacharjee^b, and Bhaskaran Muralidharan^{a*}

^aDepartment of Electrical Engineering, Indian Institute of Technology Bombay, Powai, Mumbai-400076, India

^bIndo-Korea Science and Technology Center (IKST), Jakkur, Bengaluru 560065, India and

^cElectronic Materials Research Center, KIST, Seoul 136-791, South Korea.

(Dated: January 30, 2023)

The two-dimensional compound group of MXenes, which exhibit unique optical, electrical, chemical, and mechanical properties, are an exceptional class of transition metal carbides and nitrides. In addition to traditional applications in Li-S, Li-ion batteries, conductive electrodes, hydrogen storage, and fuel cells, the low lattice thermal conductivity coupled with high electron mobility in the semiconducting oxygen-functionalized MXene Ti₂CO₂ has led to the recent interests in high-performance thermoelectric and nanoelectronic devices. Apart from the above dc- transport applications, it is crucial to also understand ac- transport across them, given the growing interest in applications surrounding wireless communications and transparent conductors. In this work, we investigate using our recently developed *ab initio* transport model, the real and imaginary components of electron mobility and conductivity to conclusively depict carrier transport beyond the room temperature for frequency ranges upto the terahertz range. We also contrast the carrier mobility and conductivity with respect to the Drude's model to depict its inaccuracies for a meaningful comparison with experiments. Our calculations show the effect of acoustic deformation potential scattering, piezoelectric scattering, and polar optical phonon scattering mechanisms. Without relying on experimental data, our model requires inputs calculated from first principles using density functional theory. Our results set the stage for providing ab-initio based ac- transport calculations given the current research on MXenes for high frequency applications.

I. INTRODUCTION

Two-dimensional (2D) materials [1–7] have unique optical, electrical, chemical, and mechanical properties and have received much attention over the last two decades due to their utility in optoelectronics [8], flexible electronics [9], nanogenerators [10], nanoelectromechanical systems [11], sensing [12] and terahertz (THz) frequency devices [13]. The 2D compound group of MXenes [14–19] are an exceptional class of transition metal carbides and nitrides. In addition to traditional applications in Li-S [20], Li-ion batteries (LIBs) [20–25], conductive electrodes, [26], hydrogen storage [27–31], optics [32–35], and fuel cells [36], the narrow bandgap, improved thermodynamic stability, high Seebeck coefficient, high figure of merit, and the low lattice thermal conductivity coupled with high electron mobility in semiconducting and oxygen-functionalized 2D MXene Ti₂CO₂ has led to the recent interests in high-performance thermoelectric (TE) [37–39] and nanoelectronic devices [40, 41]. In the past few years, different modules [42–45] have been developed to predict dc transport properties of such materials with inputs calculated from the first-principles methods.

The importance of high-frequency analysis is growing due to the applicability of MXenes in developing thin and flexible antennas and for wearable and transparent electronic devices [40, 46–49]. There are several aspects that function as restrictions, which makes it more chal-

lenging to fabricate such an antenna for wireless communication. The skin depth is one of them, which is frequency dependent. Apart from this, impedance matching is necessary, which further helps in determining the voltage standing wave ratio (VSWR). Typically, MXenes can match impedance at extremely small antenna thicknesses [41, 50]. Furthermore, the gain value depends on the thickness, and the gain values of all the MXene antennas decreases with decreasing thickness, which further emphasizes on accurate computation of frequency-dependent transport parameters. With the thickness and electrical conductivity, contributing majorly towards absorption, it is also possible to estimate the absorption loss for non-magnetic and conducting shielding materials [51].

Given the myriad possibilities for high frequency operation of MXenes, and the paucity in the development of theoretical models, we advance an extended version of our previously developed module AMMCR [52] to obtain the highly accurate frequency-dependent electrical conductivity and other high frequency transport characteristics, which paves the way for the manufacturing of a variety of flexible, wearable, and nanoelectronic devices.

Our model is based on the Rode's iterative method [53–55] evolved from the conventional semi-classical Boltzmann transport equation (BTE) [56]. We have included various scattering mechanisms explicitly. The variations in the characteristics across a wide range of temperatures, carrier concentrations, and frequencies are admirably captured by our model. Since our model does not rely on experimental data, it can predict the transport

* corresponding author: bm@ee.iitb.ac.in

parameters of any new emerging semiconducting material that is currently being developed and for which the experimental data is unavailable. The potential capabilities of our model [52, 57–59] include lower computational time, less complexity, more precision & accuracy, minimal computational expense, independent of experimental data, user-friendly, and faster convergence.

First, we will outline the Rode’s iterative methodology used in this study to evaluate the electron transport coefficients while taking into consideration the various scattering mechanisms at play in this semiconducting 2D material for high-frequency applications. Then, we will discuss the findings about Ti_2CO_2 MXene’s electron mobility and conductivity for ac electric field. In the upcoming sections, we will outline Rode’s iterative methodology developed here to evaluate the electron transport coefficients while taking into consideration the various scattering mechanisms for high-frequency applications. Then, we will discuss the findings about Ti_2CO_2 MXene’s electron mobility and conductivity for AC electric fields. All necessary *ab initio* inputs required for simulations are calculated from first-principles density functional theory (DFT) using the Vienna ab-initio Simulation Package (VASP) module without using any experimental data. Further, we investigate the temperature, carrier concentration and frequency dependence of mobility and conductivity in Ti_2CO_2 .

II. METHODOLOGY

A. Calculation of the *ab initio* parameters

We use density functional theory (DFT) to calculate the *ab initio* parameters, and DFT implemented in the plane wave code Vienna ab-initio Simulation Package (VASP) [60, 61] is used to carry out the electronic structure calculations. The projector augmented wave (PAW) [62, 63] method is used to calculate the pseudopotentials, and the generalized gradient approximation (GGA) is used to treat the exchange-correlation functional, which is parameterized by the Perdew-Burke-Ernzerhof (PBE) formalism [64]. The cut-off energy for plane waves is set at 500 eV, and for the structural optimization, the conjugate gradient algorithm is used. The energy and force convergence criteria are 10^{-6} eV and -0.01 eV/Å, respectively. The parameters needed for simulations are shown in table I. For more details on band structure and parameters needed for simulations, DOS and phonon dispersion, refer to our previous study [58].

B. Solution of the Boltzmann transport equation

Our model, which is a more evolved and advanced version of our previously developed tool AMMCR, is used to compute the transport parameters [52, 57]. The brief

Table I. Material Parameters used for Ti_2CO_2

Parameters	Values
PZ constant, e_{11} (C/m)	3×10^{-13}
Acoustic deformation potentials, $D_A(\text{eV})$:	
$D_{A,LA}$	8.6
$D_{A,TA}$	3.5
$D_{A,ZA}$	0.7
Elastic modulus, $C_A(\text{N/m})$:	
$C_{A,LA}$	301.7
$C_{A,TA}$	391.6
$C_{A,ZA}$	59.3
Polar optical phonon frequency $\omega_{POP}(\text{THz})$:	
$\omega_{POP,LO}$	3.89
$\omega_{POP,TO}$	3.89
$\omega_{POP,HP}$	8.51
High frequency dielectric constant, κ_∞	23.57
Low frequency dielectric constant, κ_0	23.6

methodology for solving the BTE is presented below. The BTE for the electron distribution function f is given by

$$\frac{\partial f(\mathbf{k})}{\partial t} + \mathbf{v} \cdot \nabla_{\mathbf{r}} f - \frac{e\mathbf{F}}{\hbar} \cdot \nabla_{\mathbf{k}} f = \left. \frac{\partial f}{\partial t} \right|_{\text{coll}}, \quad (1)$$

where \mathbf{v} is the carrier velocity, e is the electronic charge, \mathbf{F} is the applied electric field, and f represents the probability distribution function of carrier in the real and the momentum space as a function of time, $\left. \frac{\partial f}{\partial t} \right|_{\text{coll}}$ denotes the change in the distribution function with time due to the collisions. Under steady-state, $\frac{\partial f(\mathbf{k})}{\partial t} = 0$ and spatial homogeneous condition $\nabla_{\mathbf{r}} f = 0$, Eq. (1) can be written as

$$\begin{aligned} \frac{-e\mathbf{F}}{\hbar} \cdot \nabla_{\mathbf{k}} f = \int \left[s(\mathbf{k}', \mathbf{k}) f'(1-f) \right. \\ \left. - s(\mathbf{k}, \mathbf{k}') f(1-f') \right] d\mathbf{k}', \end{aligned} \quad (2)$$

where $s(\mathbf{k}, \mathbf{k}')$ denotes the transition rate of an electron from a state \mathbf{k} to a state \mathbf{k}' . For better understanding of the Rode’s algorithm [53–55, 65], refer to our previous studies [52, 57].

C. Complex mobility and conductivity

For an ac electric field $\mathbf{F} = F_0 e^{j\omega t}$, the distribution function can be expressed as [66–68]

$$f(\mathbf{k}) = f_0(k) - evF \left[\phi_r + j\phi_i \right] \left(\frac{\partial f_0}{\partial E} \right) \cos \theta_c, \quad (3)$$

where \mathbf{k} is the Bloch vector for energy E , θ_c is the angle between \mathbf{F} and \mathbf{k} . Here, $k=|\mathbf{k}|$, $F=|\mathbf{F}|$, and ϕ_r and ϕ_i are functions that can be calculated using the Boltzmann

equation. Substituting Eq. (3) in the BTE and equating the coefficient of ϕ_r and ϕ_i on two sides, we get

$$L_c \phi_r = 1 + \phi_i \omega \quad (4)$$

$$L_c \phi_i + \omega \phi_r = 0, \quad (5)$$

where L_c is the collision operator, and it is given by [69, 70]

$$L_c \phi(E) = S_o(E) \phi(E) - S_e(E) \phi(E + \hbar \omega_{pop}) - S_a(E) \phi(E - \hbar \omega_{pop}), \quad (6)$$

where $\hbar \omega_{pop}$ is the polar optical phonon (POP) energy. The term $S_o(E)$ is the sum of out-scattering rates due to the POP scattering interaction and the out-scattering and in-scattering contributions from the elastic scattering processes. Here, $S_e(E)$ and $S_a(E)$ are the in-scattering rates due to the emission and the absorption processes of the POP scattering mechanism. Separating ϕ_r and ϕ_i from (4) and (5), we get

$$\phi_r(E) = \frac{S_o(E)}{S_o^2(E) + \omega^2} [1 + S_{ar}(E) + S_{er}(E)] + \frac{\omega}{S_o^2(E) + \omega^2} [S_{ai}(E) + S_{ei}(E)] \quad (7)$$

$$\phi_i(E) = \frac{-\omega}{S_o^2(E) + \omega^2} [1 + S_{ar}(E) + S_{er}(E)] + \frac{S_o(E)}{S_o^2(E) + \omega^2} [S_{ai}(E) + S_{ei}(E)], \quad (8)$$

where $S_{ar}(E) = S_a(E) \phi_r(E - \hbar \omega_{pop})$, $S_{er}(E) = S_e(E) \phi_r(E + \hbar \omega_{pop})$, $S_{ai}(E) = S_a(E) \phi_i(E - \hbar \omega_{pop})$ and $S_{ei}(E) = S_e(E) \phi_i(E + \hbar \omega_{pop})$. Equations (7) and (8) are to be solved by the Rode's iterative method [54, 55]. After determining ϕ_r and ϕ_i , the real and imaginary components of complex conductivity are determined using the following expressions [68, 69]

$$\sigma_r = \frac{e^2 \int v^2(E) D_s(E) \phi_r(E) (\frac{\partial f_0}{\partial E}) dE}{2F} \quad (9)$$

$$\sigma_i = \frac{e^2 \int v^2(E) D_s(E) \phi_i(E) (\frac{\partial f_0}{\partial E}) dE}{2F}, \quad (10)$$

where $D_s(E)$ is the density of states (DOS). The complex mobility can be expressed as $\mu_r - j\mu_i$. The real and imaginary components of mobility are then calculated by using the following equation

$$\mu_r = \frac{\sigma_r}{N_D e} \times t_z \quad (11)$$

$$\mu_i = \frac{\sigma_i}{N_D e} \times t_z, \quad (12)$$

where N_D is the electron doping concentration and t_z denotes the thickness of the material along the z-direction, which is taken to be 4.45 Å in our calculations.

D. Scattering Mechanisms

1. Acoustic deformation potential scattering

The scattering rate of the acoustic deformation potential (ADP) scattering is defined as [38, 71, 72]

$$\frac{1}{\tau_{ADP}^\kappa(E)} = \frac{D_{\kappa A}^2 k_B T k}{\hbar^2 C_A^\kappa v}, \quad (13)$$

where k is the wave vector, C_A is the elastic modulus, T is the temperature, \hbar is the reduced Planck's constant, $D_{\kappa A}$ is acoustic deformation potential and k_B denotes the Boltzmann constant. The term v is the group velocity of the electrons, and $\kappa \in LA, TA, ZA$. The energy dependence is introduced here, via the wave vector k . We fit the lowest conduction band analytically with a six-degree polynomial to obtain a smooth curve for the group velocity. This allows us to obtain a one-to-one mapping between the wave vector k and the band energies.

2. Piezoelectric scattering

The scattering rates due to piezoelectric (PZ) scattering can be expressed as [73]

$$\frac{1}{\tau_{PZ}(E)} = \frac{1}{\tau_{ADP}(E)} \times \frac{1}{2} \times \left(\frac{e_{11} e}{\epsilon_0 D_A} \right)^2, \quad (14)$$

where ϵ_0 is vacuum permeability, and e_{11} is a piezoelectric constant (unit of C/m).

3. Polar optical phonon scattering

The inelastic scattering in the system is caused by POP scattering mechanism. The POP scattering contribution to the out-scattering is given by [67, 74]

$$S_o^{in}(k) = \frac{C_{POP}}{(1 - f_0(E))} [P + Q], \quad (15)$$

where

$$P = N_V (1 - f_0(E + \hbar \omega_{POP})) I^+(E) \frac{k^+}{v(E + \hbar \omega_{POP})} \quad (16)$$

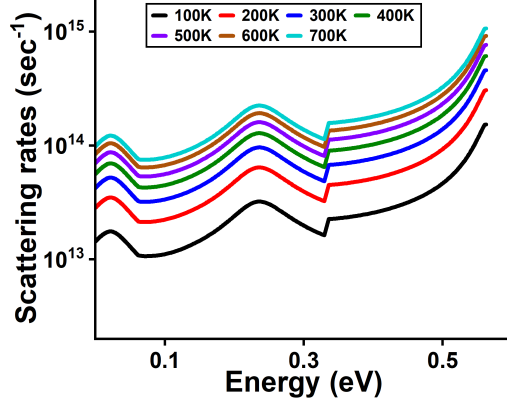


Fig. 1. Scattering rates vs. carrier energy at various temperatures with a doping concentration of $1 \times 10^{12} \text{ cm}^{-2}$.

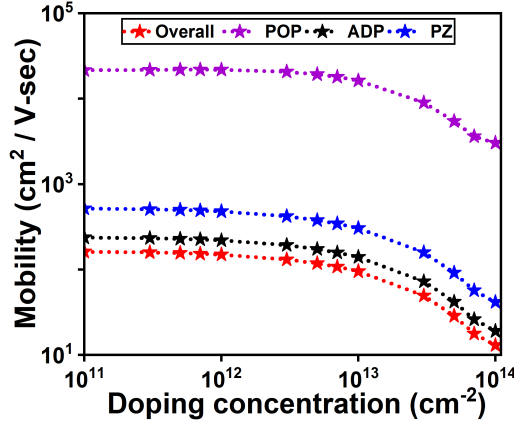


Fig. 2. Contribution to the mobility by different scattering mechanisms vs. doping concentration at room temperature with zero Hz frequency.

$$Q = (N_V + 1)(1 - f_0(E - \hbar\omega_{POP})) \times I^-(E) \frac{k^-}{v(E - \hbar\omega_{POP})} \quad (17)$$

$$I^+(E) = \int_0^{2\pi} \frac{1}{q_a} d\theta \quad (18)$$

$$I^-(E) = \int_0^{2\pi} \frac{1}{q_e} d\theta \quad (19)$$

$$q_a = (k^2 + (k^+)^2 - 2kk^+ \cos \theta) \quad (20)$$

$$q_e = (k^2 + (k^-)^2 - 2kk^- \cos \theta), \quad (21)$$

where k^+ denotes the wave vector at energy $E + \hbar\omega$ and k^- represents the wave vector at energy $E - \hbar\omega$. The angle between the initial wave vector \mathbf{k} and the final wave vector \mathbf{k}' is defined as θ .

$$C_{POP} = \frac{e^2 \omega_{POP}}{8\pi \hbar \epsilon_0} \times \left(\frac{1}{\kappa_\infty} - \frac{1}{\kappa_0} \right), \quad (22)$$

where κ_∞ and κ_0 are the high and low-frequency dielectric constants, respectively.

The sum of in-scattering rates due to the POP absorption and the emission can be used to represent the in-scattering contribution due to the POP, an inelastic and anisotropic scattering mechanism.

$$S_i^{in}(k) = S_a^{in}(k) + S_e^{in}(k), \quad (23)$$

where $S_a^{in}(k)$ denotes the in-scattering of electrons from energy $E - \hbar\omega_{POP}$ to energy E due to the absorption of polar optical phonons and $S_e^{in}(k)$ denotes the in-scattering of electrons from energy $E + \hbar\omega_{POP}$ to energy E due to the emission of polar optical phonons.

$$S_a^{in}(k) = C_{POP}(N_V + 1)f_0(E)J^-(E) \times A \quad (24)$$

$$A = \frac{k^-}{v(E - \hbar\omega_{POP})f_0(E - \hbar\omega_{POP})} \quad (25)$$

$$S_e^{in}(k) = C_{POP}(N_V)f_0(E)J^+(E) \times B \quad (26)$$

$$B = \frac{k^+}{v(E + \hbar\omega_{POP})f_0(E + \hbar\omega_{POP})} \quad (27)$$

$$N_V = \frac{1}{\exp(\hbar\omega_{POP}/k_B T) - 1} \quad (28)$$

$$J^+(E) = \int_0^{2\pi} \frac{\cos \theta}{q_{i,e}} d\theta \quad (29)$$

$$J^-(E) = \int_0^{2\pi} \frac{\cos \theta}{q_{i,a}} d\theta \quad (30)$$

$$q_{i,a} = [(k^-)^2 + k^2 - 2kk^- \cos \theta] \quad (31)$$

$$q_{i,e} = [(k^+)^2 + k^2 - 2kk^+ \cos \theta]. \quad (32)$$

We replace the term $\frac{\hbar k}{m^*}$ by the group velocity [52, 57] while deriving the expression for different scattering rates, which we calculate using the DFT band structure [52, 57].

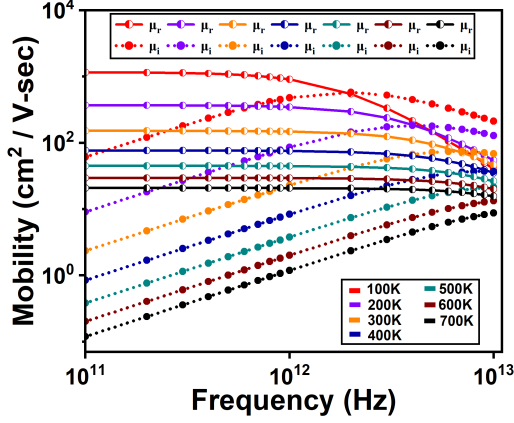


Fig. 3. Variation of the real and the imaginary components of mobility as a function of frequency for various temperatures with a doping concentration of $1 \times 10^{12} \text{ cm}^{-2}$.

III. RESULTS AND DISCUSSION

In Fig. 1, we show the total scattering rates, which is the sum of three scattering mechanisms we have considered in Ti_2CO_2 . These three scattering mechanisms are the POP scattering, the PZ scattering, and the ADP scattering mechanisms. Scattering rates increase as we increase the temperature and hence the mobility decreases with an increase in the temperature.

In Fig. 2 we show the contribution to the mobility due to the ADP, the POP, and the PZ scattering mechanisms. Here, in Ti_2CO_2 , the ADP scattering makes the most significant contribution followed by the PZ scattering mechanism and the POP scattering mechanism has the least effect. Therefore, the mobility and the conductivity in Ti_2CO_2 is mainly limited by the ADP scattering and hence acoustic phonons are the primary limiters of the conductivity and the mobility. Refer to our previous study [58] where we have computed the scattering rates due to the individual acoustic phonons for better understanding the nature of acoustic phonons that limit the conductivity in Ti_2CO_2 .

In our previous study, we demonstrated that the longitudinal acoustic (LA) phonons play an important role in Ti_2CO_2 . Therefore, the ADP and the PZ scattering are the two primary carrier scattering processes involved in Ti_2CO_2 . As expected, the mobility decrease with increasing electron concentration. The mobility values are not significantly different for low electron concentrations, i.e., within the range $[1 \times 10^{11} \text{ cm}^{-2} - 1 \times 10^{13} \text{ cm}^{-2}]$. However, there is a sharp reduction in the mobility, as shown in Fig. 2, at electron concentrations greater than $1 \times 10^{13} \text{ cm}^{-2}$. Consider Matthiessen's rule (33) to understand the mobility trend in relation to temperature and the carrier concentration, which can be expressed as

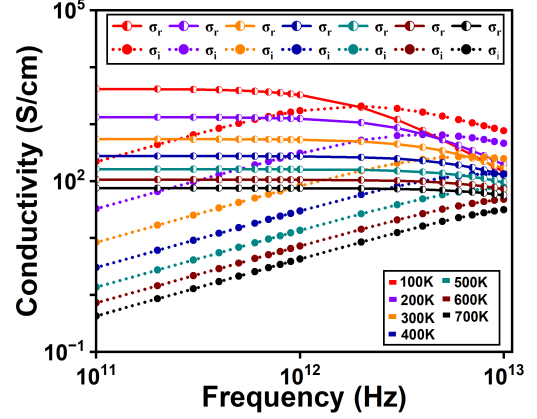


Fig. 4. Variation of the real and the imaginary components of conductivity as a function of frequency for various temperatures with a doping concentration of $1 \times 10^{12} \text{ cm}^{-2}$.

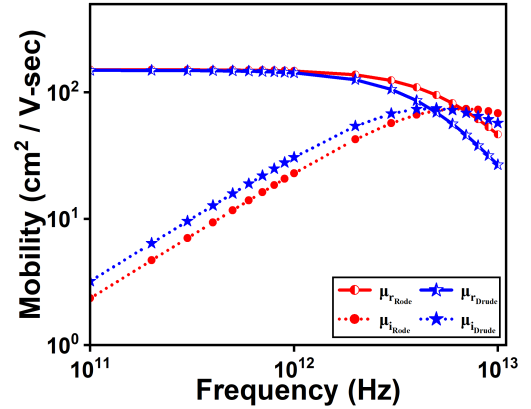


Fig. 5. Comparison of mobility (i.e., the real and the imaginary components) with the Rode's and the Drude's method at 300 K for doping concentration of $1 \times 10^{12} \text{ cm}^{-2}$.

$$\frac{1}{\mu} = \frac{1}{\mu_{ADP}} + \frac{1}{\mu_{PZ}} + \frac{1}{\mu_{POP}}, \quad (33)$$

where μ stands for total mobility. Equation (33) states that the circumstance where the component with the lowest value is the most significant derives from the reciprocal relationship between the overall mobility and individual components. In Fig. 2, we show that the acoustic mode has the dominant contribution at all doping concentrations however, as demonstrated in Fig. 2, the PZ scattering mechanism significantly contributes across the entire doping range.

In Fig. 3, we show that as the temperature rises from 100 K to 700 K, both μ_r and μ_i for $N_D = 1 \times 10^{12} \text{ cm}^{-2}$ decreases and these findings are explained by the fact

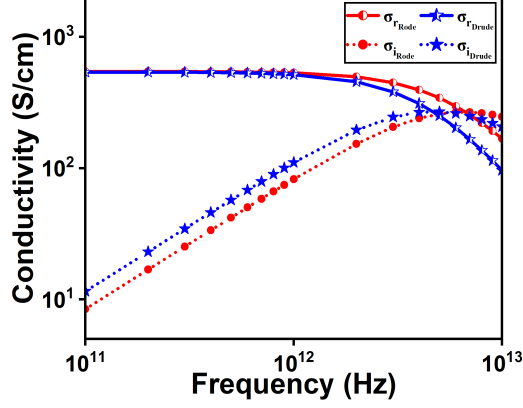


Fig. 6. Comparison of conductivity (i.e., the real and the imaginary components) with the Rode's and the Drude's method at 300 K for doping concentration of $1 \times 10^{12} \text{ cm}^{-2}$.

that the scattering rate increases with increasing temperature. Figure 3 depicts the crossover between μ_r and μ_i at a specific frequency for each temperature, with the crossover shifting towards a higher frequency as the temperature increases. It is worth pointing that high-frequency effects are stronger at temperatures below the room temperature. Figure 4 shows the decrease in the conductivity caused by a reduction in mobility with an increase in temperature. In Fig. 5, we compare the mobility calculated using the Rode's iterative method to the mobility calculated using the Drude's theory. The Drude's mobility can be expressed as [75]

$$\mu_r = \frac{(e\tau/m^*)}{(1 + \omega^2\tau^2)} \quad (34)$$

$$\mu_i = \frac{(e\omega\tau^2/m^*)}{(1 + \omega^2\tau^2)} \quad (35)$$

Using the DFT, we calculate m^*/m_0 , which is 0.4010, where m_0 is the rest mass of an electron. In order to determine the mobility using the Drude's approach, we first determine τ value at $\omega = 0$ using μ_r as $1.496985 \times 10^2 \text{ cm}^2/\text{V-sec}$, calculated at $T = 300 \text{ K}$ and doping value of $1 \times 10^{12} \text{ cm}^{-2}$. The calculated τ value is 3.4134×10^{-14} seconds. By adjusting the value of ω while keeping τ fixed at 3.4134×10^{-14} seconds, we calculate the real and the imaginary components of mobility.

Figure 5 shows that the Drude's values are close to exact values and that mobility can be estimated using the Drude's model unless high accuracy is required. But at higher frequencies, there is a significant deviation in the real component of mobility, and the Rode's method provides more accurate results. We also show the comparison of conductivity in Ti_2CO_2 calculated using the Rode's and the Drude's approach in a manner similar to

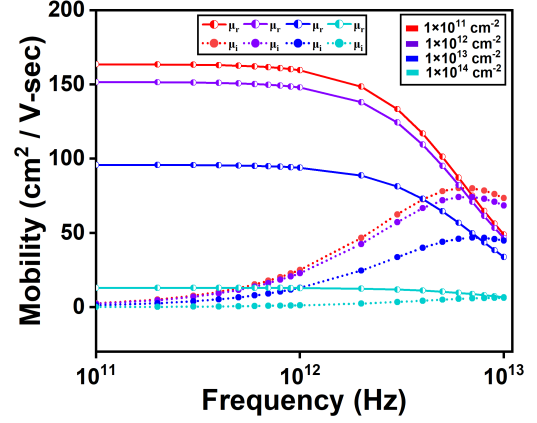


Fig. 7. Variation of the real and the imaginary components of the room temperature mobility as a function of frequency for various doping concentrations.

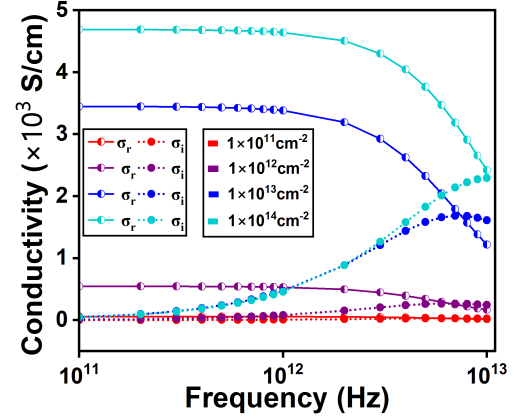


Fig. 8. Variation of the real and the imaginary components of conductivity as a function of frequency for various doping concentrations at room temperature.

that of the mobility. The calculation of Drude's conductivity is straight forward using Eqs. (11) & (12). As shown in Fig. 6, Drude's values for the real conductivity are relatively close to the exact values for the conductivity and hence the Drude's method can be used to predict the mobility unless a high degree of accuracy is not required. At higher frequencies, a considerable variation has been seen, as a result the Rode's approach is more faithful at higher frequencies.

In the Drude's model, the effect of all scattering mechanisms is merged together in a single constant relaxation time. This simplification makes all the calculations easy however, this method has some disadvantages (i) τ is obtained by fitting the experimental results to the mobility, which limits the predictability of this model. (ii) Due to over simplification of scattering mechanisms, it may lead

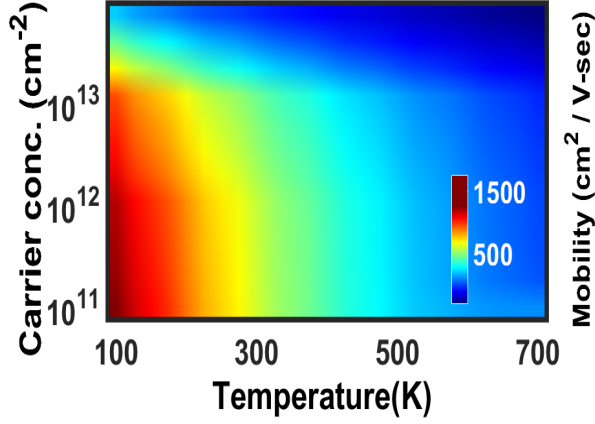


Fig. 9. Mobility vs. temperature and carrier concentration at 100 GHz frequency.

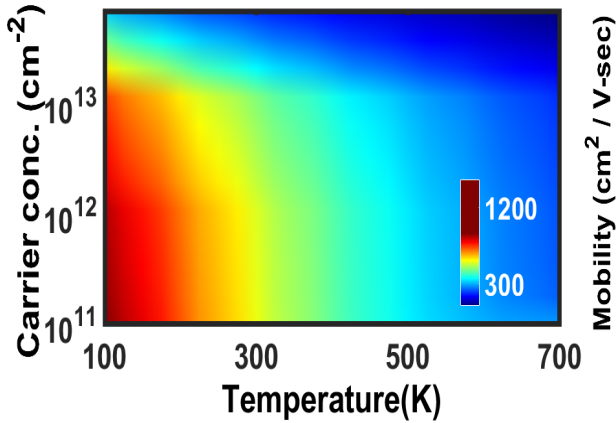


Fig. 10. Mobility vs. temperature and carrier concentration at 1 THz frequency.

to inaccurate results. (iii) It does not provide any insight into which scattering mechanisms are playing the major role. Instead, we have calculated all required inputs from the DFT without relying on any experimental data, included all scattering mechanisms explicitly and provided an insight regarding which scattering mechanisms are physically relevant to the considered semiconductor. Hence, our approach can be used to predict the mobility and the conductivity of even new emerging materials accurately. This paves the way for researchers in designing semiconductors with highly accurate transport properties based on theoretical predictions.

Figure 7 shows that μ_r remains constant at room temperature up to a frequency of around 500 GHz. Beyond this frequency, μ_r falls while μ_i rises to a maximum and then falls. The simple Drude's expressions easily predict this type of behavior. Figure 7 also shows that the mobility decreases as doping concentration increases. Figure 8 depicts the increase in the conductivity caused by an increase in carrier concentration. For low values of frequency, σ_r and σ_i are nearly constant whereas at higher frequencies, above 10^{12} Hz, σ_r decreases significantly while σ_i increases. Figures 9 and 10 depict the mobility vs. temperature and carrier concentration at frequencies of 100 GHz and 1 THz, respectively. It is clear from both the figures that the mobility decreases as the frequency value increases and mobility increases as the carrier concentration and temperature decrease.

IV. CONCLUSION

In this work, we investigated using our recently developed *ab initio* transport model, the real and imaginary components of electron mobility and conductivity to conclusively depict carrier transport beyond the room temperature for frequency ranges upto the terahertz range. We also contrasted the carrier mobility and conductivity with respect to the Drude model to depict its inaccuracies for a meaningful comparison with experiments. Our calculations showed the effect of acoustic deformation potential scattering, piezoelectric scattering, and polar optical phonon scattering mechanisms. Without relying on experimental data, our model requires inputs calculated from first principles using density functional theory. Our results set the stage for providing ab-initio based ac-transport calculations given the current research on MXenes for high frequency applications.

ACKNOWLEDGMENTS

The authors gratefully acknowledge the funding from Indo-Korea Science and Technology Center (IKST), Bangalore. The author BM wishes to acknowledge the financial support from the Science and Engineering Research Board (SERB), Government of India, under the MATRICS grant.

CODE AVAILABILITY

The code used in this work is made available at <https://github.com/anup12352/AMMCR>.

[1] R. Mas-Balleste, C. Gomez-Navarro, J. Gomez-Herrero, and F. Zamora, *Nanoscale* **3**, 20 (2011).

[2] K. S. Novoselov, A. K. Geim, S. V. Morozov, D.-e. Jiang, Y. Zhang, S. V. Dubonos, I. V. Grigorieva, and A. A.

- Firsov, *science* **306**, 666 (2004).
- [3] A. K. Geim, *science* **324**, 1530 (2009).
 - [4] A. K. Geim and K. S. Novoselov, in *Nanoscience and technology: a collection of reviews from nature journals* (World Scientific, 2010), pp. 11–19.
 - [5] A. C. Neto, F. Guinea, N. M. Peres, K. S. Novoselov, and A. K. Geim, *Reviews of modern physics* **81**, 109 (2009).
 - [6] K. S. Novoselov, D. Jiang, F. Schedin, T. Booth, V. Khotkevich, S. Morozov, and A. K. Geim, *Proceedings of the National Academy of Sciences* **102**, 10451 (2005).
 - [7] D. Akinwande, C. J. Brennan, J. S. Bunch, P. Egberts, J. R. Felts, H. Gao, R. Huang, J.-S. Kim, T. Li, Y. Li, et al., *Extreme Mechanics Letters* **13**, 42 (2017).
 - [8] J. Cheng, C. Wang, X. Zou, and L. Liao, *Advanced Optical Materials* **7**, 1800441 (2019).
 - [9] S. J. Kim, K. Choi, B. Lee, Y. Kim, and B. H. Hong, *Annual Review of Materials Research* **45**, 63 (2015).
 - [10] Z. L. Wang and J. Song, *Science* **312**, 242 (2006).
 - [11] J. Lee, Z. Wang, K. He, R. Yang, J. Shan, and P. X.-L. Feng, *Science advances* **4**, eaao6653 (2018).
 - [12] Y. Cai, J. Shen, G. Ge, Y. Zhang, W. Jin, W. Huang, J. Shao, J. Yang, and X. Dong, *ACS nano* **12**, 56 (2018).
 - [13] I.-T. Lin and J.-M. Liu, *IEEE Journal of Selected Topics in Quantum Electronics* **20**, 122 (2013).
 - [14] M. W. Barsoum, *Progress in solid state chemistry* **28**, 201 (2000).
 - [15] M. W. Barsoum and M. Radovic, *Annual review of materials research* **41**, 195 (2011).
 - [16] M. Naguib, M. Kurtoglu, V. Presser, J. Lu, J. Niu, M. Heon, L. Hultman, Y. Gogotsi, and M. W. Barsoum, *Advanced materials* **23**, 4248 (2011).
 - [17] M. Naguib, O. Mashtalir, J. Carle, V. Presser, J. Lu, L. Hultman, Y. Gogotsi, and M. W. Barsoum, *ACS nano* **6**, 1322 (2012).
 - [18] M. Naguib, V. N. Mochalin, M. W. Barsoum, and Y. Gogotsi, *Advanced materials* **26**, 992 (2014).
 - [19] M. Ghidui, M. Naguib, C. Shi, O. Mashtalir, L. Pan, B. Zhang, J. Yang, Y. Gogotsi, S. J. Billinge, and M. W. Barsoum, *Chemical communications* **50**, 9517 (2014).
 - [20] X. Liang, A. Garsuch, and L. F. Nazar, *Angewandte Chemie* **127**, 3979 (2015).
 - [21] M. Naguib, J. Come, B. Dyatkin, V. Presser, P.-L. Taberna, P. Simon, M. W. Barsoum, and Y. Gogotsi, *Electrochemistry Communications* **16**, 61 (2012).
 - [22] Y. Tian, Y. An, and J. Feng, *ACS applied materials & interfaces* **11**, 10004 (2019).
 - [23] Y. Xie, M. Naguib, V. N. Mochalin, M. W. Barsoum, Y. Gogotsi, X. Yu, K.-W. Nam, X.-Q. Yang, A. I. Kolesnikov, and P. R. Kent, *Journal of the American Chemical Society* **136**, 6385 (2014).
 - [24] Q. Tang, Z. Zhou, and P. Shen, *Journal of the American Chemical Society* **134**, 16909 (2012).
 - [25] D. Er, J. Li, M. Naguib, Y. Gogotsi, and V. B. Shenoy, *ACS applied materials & interfaces* **6**, 11173 (2014).
 - [26] J. Halim, M. R. Lukatskaya, K. M. Cook, J. Lu, C. R. Smith, L.-Å. Näslund, S. J. May, L. Hultman, Y. Gogotsi, P. Eklund, et al., *Chemistry of Materials* **26**, 2374 (2014).
 - [27] Q. Hu, D. Sun, Q. Wu, H. Wang, L. Wang, B. Liu, A. Zhou, and J. He, *The Journal of Physical Chemistry A* **117**, 14253 (2013).
 - [28] P. Kumar, S. Singh, S. Hashmi, and K.-H. Kim, *Nano Energy* **85**, 105989 (2021).
 - [29] J.-C. Lei, X. Zhang, and Z. Zhou, *Frontiers of Physics* **10**, 276 (2015).
 - [30] X. Li, C. Wang, Y. Cao, and G. Wang, *Chemistry–An Asian Journal* **13**, 2742 (2018).
 - [31] Q. Hu, H. Wang, Q. Wu, X. Ye, A. Zhou, D. Sun, L. Wang, B. Liu, and J. He, *International journal of hydrogen energy* **39**, 10606 (2014).
 - [32] Y. Wang, Y. Xu, M. Hu, H. Ling, and X. Zhu, *Nanophotonics* **9**, 1601 (2020).
 - [33] X. Jiang, A. V. Kuklin, A. Baev, Y. Ge, H. Ågren, H. Zhang, and P. N. Prasad, *Physics Reports* **848**, 1 (2020).
 - [34] B. Fu, J. Sun, C. Wang, C. Shang, L. Xu, J. Li, and H. Zhang, *Small* **17**, 2006054 (2021).
 - [35] Q. Xue, H. Zhang, M. Zhu, Z. Pei, H. Li, Z. Wang, Y. Huang, Y. Huang, Q. Deng, J. Zhou, et al., *Advanced Materials* **29**, 1604847 (2017).
 - [36] X. Xie, S. Chen, W. Ding, Y. Nie, and Z. Wei, *Chemical Communications* **49**, 10112 (2013).
 - [37] A. N. Gandi, H. N. Alshareef, and U. Schwingenschlögl, *Chemistry of Materials* **28**, 1647 (2016).
 - [38] X.-H. Zha, Q. Huang, J. He, H. He, J. Zhai, J. S. Francisco, and S. Du, *Scientific reports* **6**, 1 (2016).
 - [39] S. Sarikurt, D. Çakır, M. Keçeli, and C. Sevik, *Nanoscale* **10**, 8859 (2018).
 - [40] H. Kim and H. N. Alshareef, *ACS Materials Letters* **2**, 55 (2019).
 - [41] A. Sarycheva, A. Polemi, Y. Liu, K. Dandekar, B. Anasori, and Y. Gogotsi, *Science advances* **4**, eaau0920 (2018).
 - [42] G. K. Madsen and D. J. Singh, *Computer Physics Communications* **175**, 67 (2006).
 - [43] S. Poncé, E. R. Margine, C. Verdi, and F. Giustino, *Computer Physics Communications* **209**, 116 (2016).
 - [44] A. Faghaninia, J. W. Ager III, and C. S. Lo, *Physical Review B* **91**, 235123 (2015).
 - [45] A. M. Ganose, J. Park, A. Faghaninia, R. Woods-Robinson, K. A. Persson, and A. Jain, *Nature communications* **12**, 1 (2021).
 - [46] B. Sindhu, V. Adepu, P. Sahatiya, and S. Nandi, *FlatChem* **33**, 100367 (2022).
 - [47] S. Lee, E. H. Kim, S. Yu, H. Kim, C. Park, S. W. Lee, H. Han, W. Jin, K. Lee, C. E. Lee, et al., *ACS nano* **15**, 8940 (2021).
 - [48] C. Ma, M.-G. Ma, C. Si, X.-X. Ji, and P. Wan, *Advanced Functional Materials* **31**, 2009524 (2021).
 - [49] C. J. Zhang and V. Nicolosi, *Energy Storage Materials* **16**, 102 (2019).
 - [50] D. M. Pozar (2009).
 - [51] A. Iqbal, P. Sambyal, and C. M. Koo, *Advanced Functional Materials* **30**, 2000883 (2020).
 - [52] A. K. Mandia, B. Muralidharan, J.-H. Choi, S.-C. Lee, and S. Bhattacharjee, *Computer Physics Communications* **259**, 107697 (2021).
 - [53] D. Rode, *Physical Review B* **2**, 1012 (1970).
 - [54] D. Rode, *physica status solidi (b)* **55**, 687 (1973).
 - [55] D. Rode, in *Semiconductors and semimetals* (Elsevier, 1975), vol. 10, pp. 1–89.
 - [56] M. Lundstrom, *Fundamentals of carrier transport* (2002).
 - [57] A. K. Mandia, R. Patnaik, B. Muralidharan, S.-C. Lee, and S. Bhattacharjee, *Journal of Physics: Condensed Matter* **31**, 345901 (2019).
 - [58] A. K. Mandia, N. A. Koshi, B. Muralidharan, S. C. Lee, and S. Bhattacharjee, *Journal of Materials Chemistry C* (2022).

- [59] R. Kumar, A. K. Mandia, A. Singh, and B. Muralidharan, arXiv preprint arXiv:2301.04858 (2023).
- [60] G. Kresse and J. Furthmüller, Computational materials science **6**, 15 (1996).
- [61] G. Kresse and J. Furthmüller, Physical Review B **54**, 11169 (1996).
- [62] P. E. Blöchl, Physical Review B **50**, 17953 (1994).
- [63] G. Kresse and D. Joubert, Physical Review B **59**, 1758 (1999).
- [64] J. P. Perdew, K. Burke, and M. Ernzerhof, Physical Review Letters **77**, 3865 (1996).
- [65] D. Rode, Physical Review B **2**, 4036 (1970).
- [66] A. Ghosal, D. Chattopadhyay, and N. Purkai, physica status solidi (a) **73**, K119 (1982).
- [67] B. R. Nag, *Electron transport in compound semiconductors*, vol. 11 (Springer Science & Business Media, 2012).
- [68] B. Nag and G. Dutta, physica status solidi (b) **71**, 401 (1975).
- [69] B. Nag, Journal of Applied Physics **46**, 4819 (1975).
- [70] D. Howarth and E. H. Sondheimer, Proceedings of the Royal Society of London. Series A. Mathematical and Physical Sciences **219**, 53 (1953).
- [71] E. Hwang and S. D. Sarma, Physical Review B **77**, 115449 (2008).
- [72] I.-T. Lin, Y.-P. Lai, K.-H. Wu, and J.-M. Liu, Applied Sciences **4**, 28 (2014).
- [73] K. Kaasbjerg, K. S. Thygesen, and A.-P. Jauho, Physical Review B **87**, 235312 (2013).
- [74] T. Kawamura and S. D. Sarma, Physical review B **45**, 3612 (1992).
- [75] D. Chattopadhyay, Journal of Applied Physics **51**, 1850 (1980).